

Nanopipette Fabrication Guidelines for SICM Nanoscale Imaging

Yasufumi Takahashi,* Yuya Sasaki, Takeshi Yoshida, Kota Honda, Yuanshu Zhou, Takafumi Miyamoto, Tomoko Motoo, Hiroki Higashi, Andrew Shevchuk, Yuri Korchev, Hiroki Ida, Rikinari Hanayama, and Takeshi Fukuma



Cite This: *Anal. Chem.* 2023, 95, 12664–12672



Read Online

ACCESS |



Metrics & More

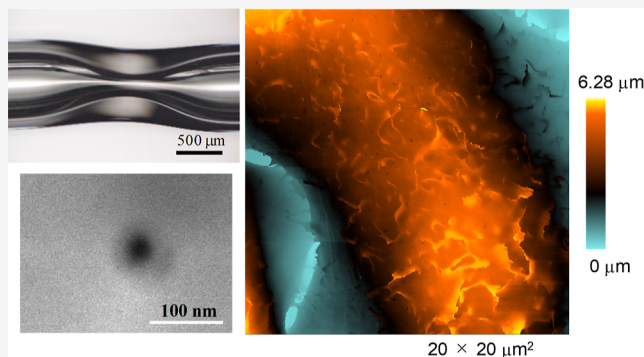


Article Recommendations



Supporting Information

ABSTRACT: Scanning ion conductance microscopy (SICM) is a promising tool for visualizing the dynamics of nanoscale cell surface topography. However, there are still no guidelines for fabricating nanopipettes with ideal shape consisting of small apertures and thin glass walls. Therefore, most of the SICM imaging has been at a standstill at the submicron scale. In this study, we established a simple and highly reproducible method for the fabrication of nanopipettes with sub-20 nm apertures. To validate the improvement in the spatial resolution, we performed time-lapse imaging of the formation and disappearance of endocytic pits as a model of nanoscale time-lapse topographic imaging. We have also successfully imaged the localization of the hot spot and the released extracellular vesicles. The nanopipette fabrication guidelines for the SICM nanoscale topographic imaging can be an essential tool for understanding cell–cell communication.



INTRODUCTION

The spatial resolution of live cell imaging is one of the most important factors to understand cell structure and function. Super-resolution microscopy enables the visualization of the dynamic morphology of cells at the submicron scale. For example, lattice light sheet microscopy was used to visualize the dynamics of micropinocytosis.^{1,2} However, visualizing the endocytosis process is still difficult because of the spatial resolution issue.

Scanning ion conductance microscopy (SICM) is a live cell topography imaging tool for visualizing the dynamic nanoscale structure changes without labeling.^{3–7} SICM uses glass nanopipettes as scanning probes for topographic imaging and has been used to visualize the nanoscale topography of cardiac myocyte,⁸ neuron,^{9–12} kidney,¹³ cancer,^{14,15} hair,¹⁶ and lung cells.¹⁷ The combination of SICM with fluorescence imaging techniques is effective in identifying the structure-specific localization of biomolecules on the cell surface.^{8,18–21} The improvement of scanning speed is one of the hot topics of SICM system development.^{10,15,17,22–24} Limited by the temporal resolution of the current amplifier, the nanopipette aperture size has to be adjusted. If imaging speed is a priority, the spatial resolution must be compromised by making the nanopipette slightly larger. The internalization process of the nanoparticle on a live cell is essential to cell membrane phenomena and a desirable target for SICM imaging. Previously, SICM has been used for visualizing the endocytosis process²⁵ and nanoparticle internalization.^{17,26} A cap formation process during clathrin-dependent endocytosis was a new

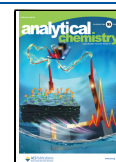
finding enabled by SICM imaging. SICM time-lapse imaging of the cap formation requires nanopipettes with thin glass walls as small cell surface structures can be deformed when using thick glass nanopipettes. A lack of guidelines for reproducibly fabricating nanopipettes with sub-20 nm apertures with thin glass walls prevents SICM's widespread use for time-lapse imaging of the cap formation.

A nanopipette with a small aperture and a thin glass wall is necessary for improving the SICM spatial resolution. High-resolution SICM was reported for the visualization of the 6 nm periodic structure of the S-layer protein using a quartz nanopipette.²⁷ The melting temperature of quartz glass is higher than that of borosilicate glass, providing a better control of the pulling process on a laser puller. Therefore, the fabrication of a quartz nanopipette with a small aperture and thin glass wall capillaries is easier than with the borosilicate ones. The optimization of these factors was established by patch clamp researchers.²⁸ However, a particular protocol is required to fill the nanopipette with an aqueous solution due to the surface hydrophobicity of the quartz glass,^{29–31} and the quartz capillary is expensive compared to the borosilicate glass

Received: March 7, 2023

Accepted: July 28, 2023

Published: August 21, 2023



capillary. To overcome these issues, we established a new fabrication method that enables easy and reliable fabrication of borosilicate nanopipettes with a sub-20 nm radius.

Extracellular vesicles (EVs) are implicated in cellular homeostasis and cell–cell communication.^{32,33} Especially, small extracellular vesicles (small EVs) with a diameter of 40–150 nm have attracted attention for therapeutic and diagnostic applications.³⁴ The size of the small EV is smaller than the limit of conventional optical microscopy; therefore, super-resolution microscopy^{35,36} and atomic force microscopy^{37–39} are used to visualize the small EVs. However, it is still difficult to image single small EV release to characterize cell–cell communication. Shirasaki and co-workers developed the linking method of released position and released protein detection method by capturing the protein on the substrate surface close to the cell.⁴⁰

In this study, we established the guidelines for fabricating nanopipettes with sub-20 nm apertures that enabled us to visualize the nanoscale topography of the endocytic pit and the released EVs at a single particle level. Furthermore, we used SICM and confocal microscopy to visualize released small EVs at a single particle level and the localization of the hot spot.

MATERIALS AND METHODS

SICM Setup. The SICM setup was as described in our previous report.⁴¹ The glass nanopipettes were fabricated from a borosilicate glass capillary (inner diameter (ID) 0.58 mm and outer diameter (OD) 1.00 mm) (GC100F-15, Harvard Apparatus) using a CO₂ laser puller (Model P-2000, Sutter Instruments). To miniaturize the nanopipette, we controlled the ID and OD of the nanopipette in advance. The details of the nanopipette fabrication method are described in the [Results and Discussion](#) section. The nanopipettes were filled with the same sample immersion solution, and Ag/AgCl electrodes were inserted into them. The applied voltage (+0.2 V) generated an ionic flow through the tip that was used as a feedback signal.

The ion current was measured using a homemade 1 G Ω feedback resistance current amplifier. The probe was placed close to the sample by using a stepping motor (KXC06030-GC, SURUGA SEIKI) and the homemade Z-piezo stage. The stepping motor with the Z-piezo stage was implemented on a manually operated XYZ manipulator (BSS76-60C, SURUGA SEIKI) with the travel range of ± 6.5 mm. The precise probe position was controlled by XY- and Z-piezo stages. The scanning algorithms were controlled by a program written using LabVIEW2014 (National Instruments). The field-programmable gate array (National Instruments, NI USB-7856 OEM) was compiled using programs developed by us. The measurement was conducted on an optical microscope (Nikon, ECLIPSE Ti-S) placed on an antivibration table (Herz, TS-150).

SICM imaging was performed using the hopping mode.^{11,16,42} The hopping amplitude was 1–3 μm . The waiting time after the lateral movement was 1.0 ms. During this time, a reference current, I_{REF} , was measured as the average of the DC current through the probe. The probe falling and withdrawing speed were 100–320 and 1200 nm/ms, respectively. The set point was 99.7–99.3% of I_{REF} . SICM images were processed and analyzed with Gwyddion and a homemade program.

Cell Preparation. 293T cells (ATCC, CRL-3216), 293 cells (ATCC, CRL-1573), and B16F10 cells (ATCC, CRL-

6475) were maintained at 37 °C and 5% CO₂ in DMEM and 10% heat-inactivated fetal bovine serum (FBS) supplemented with penicillin and streptomycin. Human CD63 gene, pHluorin gene, and monomeric DsRed [red fluorescent protein (RFP)] gene were amplified by polymerase chain reaction from cDNA of K562 cells, pCMV-lyso-pHluorin (Addgene, 70113), and Lamp1-RFP (Addgene, 1817), respectively. The pcDNA-hCD63pHluorinRFP plasmid was generated by inserting a fusion gene of human CD63, pHluorin, and RFP into a site between *EcoRI* and *KpnI* of pcDNA3.1(–) using the Gibson Assembly System (NEB; New England Biolabs). Then, the pcDNA-hCD63pHluorinRFP plasmid was digested with *ScaI* (NEB) and transfected into 293 cells using FuGENE6 (Promega). Three days after transfection, the cells were cultured for 2 weeks in 1 mg/mL G418/DMEM–10% FBS to establish 293 CD63pHluorinRFP cells.

Preparation of EVs for SICM Imaging. The EV-depleted FBS was prepared by rotating a mixture of 5 volume of FBS with 1 volume of 50% polyethylene glycol-10,000 (Sigma-Aldrich) for 3 h and centrifuging the mixture at 1500g, 4 °C for 30 min to remove a pellet including EVs. To isolate EVs, 293T or B16F10 cells were seeded at 8×10^6 cells on a 150 mm dish and cultured for 2 days in Advanced DMEM (Thermo Fisher Scientific) with 2% EV-depleted FBS. The cultured supernatant was centrifuged at 300g, 4 °C for 5 min, 2000g, 4 °C for 20 min, and 10,000g, 4 °C for 30 min to remove the cells, cellular debris, and large EVs, respectively. The supernatant centrifuged at 10,000g (10 K sup) was subjected to imaging under SICM or further isolation of highly pure EVs. The highly pure EVs were recovered from the 10 K sup by using the TIM4-affinity method.⁴³ The isolated EVs were sealed in a dialysis membrane MWCO 3.5k (Repligen) and stirred in PBS(–) (137 mM NaCl, 8.1 mM Na₂HPO₄, 2.68 mM KCl, and 1.47 mM KH₂PO₄, pH7.4) overnight to change the buffer. The concentration of the EVs was determined in a nano-tracking analysis (NTA) by using a NanoSIGHT NS300 (Malvern, UK). After diluting the EVs with PBS(–) in the range between 1 and 10×10^8 particles/mL, the movement of EVs was recorded for 30 s at the camera level 15 and analyzed by setting the detection threshold 4.

Non-treated Petri dishes, 35 mm (Thermo Fisher Scientific), were coated with 2 mL of 1 $\mu\text{g/mL}$ mouse TIM4-Fc protein/bicarbonate buffer (71.4 mM NaHCO₃/28.6 mM Na₂CO₃, pH9.6) at 4 °C overnight. After blocking the dishes with 1% bovine serum albumin (BSA) at room temperature for 1 h, 2 mL of 10 K sup or highly pure EVs suspended in TBS-TCa (2 mM CaCl₂/0.002% Tween 20/TBS) was added to the TIM4-Fc-coated dishes and incubated at 4 °C overnight to capture EVs. The dishes were washed twice with 2 mL of TBS-TCa at each step. The EVs immobilized on dishes were imaged using the SICM. Mouse TIM4-Fc proteins were purchased from FUJIFILM Wako Pure Chemical Corporation.

Imaging EVs under Confocal Microscopy. Tissue-cultured 4-room 35 mm glass-bottom dishes (Griener) were coated with 1 $\mu\text{g/mL}$ mouse TIM4-Fc protein/PBS(–) 400 $\mu\text{L/well}$ at 4 °C overnight. After blocking the dishes with 1% BSA at room temperature for 1 h, 4×10^4 cells of 293 CD63-pHluorinRFP cells, 0.8 μL of Red Fluorochrome 635-conjugated anti-CD63 antibody (clone 3-13, FUJIFILM Wako Pure Chemical Corporation), and 400 μL of Advanced DMEM with 2% EV-depleted FBS were added to the well. The dishes were centrifuged at 400g for 3 min to make the cells

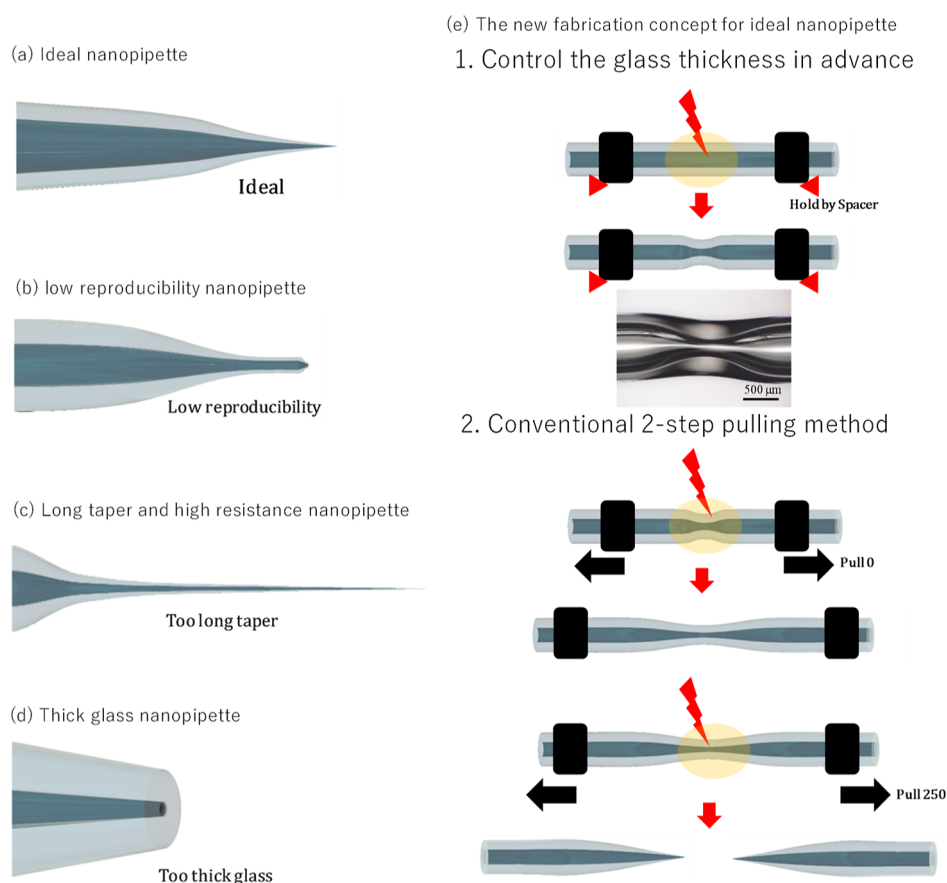


Figure 1. Different shapes of nanopipettes. (a) Ideal, (b) low reproducible, (c) long taper, and (d) thick glass nanopipettes. (e) Scheme of the new fabrication method for controlling the glass ID/OD ratio in advance.

attached to the dishes. Then, the EV secretion from the cells was imaged under a confocal microscope ECLIPSE Ti2 (Nikon) with a Dragonfly (Oxford Instruments), a CFI Plan Apo IR 60XWI lens (NA = 1.27, Nikon), and a stage top incubator STX (TOKAI HIT).

RESULTS AND DISCUSSION

Fabrication and Characterization of the Nanopipette.

During the pulling process of the glass capillary used for the nanopipette fabrication, the diameter of the glass capillary becomes smaller, and the glass wall thickness of the glass capillary becomes thinner, eventually, at the point when the glass wall runs out, separating one glass capillary into two nanopipettes. The tip aperture becomes smaller as the glass becomes thinner during the pulling process, so the size of the nanopipette aperture depends on the ratio of the initial ID to OD of the glass capillary. The smaller the ID and the larger the ID/OD ratio (thicker glass) of the initial shape of the glass capillary, the smaller the capillary can be fabricated. However, there is a limited choice in the ID/OD ratio of the glass capillaries available on the market. Therefore, we adjusted the ID of the capillary and the ID/OD ratio in advance by preheating the glass capillary. Heating shrinks the glass, making the ID smaller and the glass wall thicker. The higher the heating temperature, the greater the glass deformation due to heating (Figure 2), thus enabling the fabrication of thinner capillaries.

A two-step program of the P-2000 puller was generally used to fabricate the borosilicate nanopipette for SICM. The parameters used in this paper are shown below.

HEAT 310 FIL 3 VEL 25 DEL 150 PUL.

HEAT 280 FIL 2 VEL 23 DEL 150 PUL 250.

The resistance of the nanopipette can be modeled as two components.^{3,7} One is the pipette resistance, which is dependent on the length of the elongated glass part (shunt) at the tip of the glass nanopipette. Another is the access resistance, which is dependent on the movement of ions at the aperture of the pipette. The access resistance changes with the nanopipette–sample distance. Figure 1 shows the typical shape of the SICM nanopipette. An ideal shape of the nanopipette for SICM imaging consists of a short shunt and small aperture (Figure 1a). When the puller parameters do not adjust well, the tip of the nanopipette shape changes steeply (Figure 1b). This is because the glass is cooled down during the pulling process of the second step. In this case, the heat or velocity parameters of the second step need to be adjusted. If the heat and velocity values are too high, a long shunt nanopipette is fabricated (Figure 1c). The long taper nanopipette shows an unstable and rectified ion current.^{44–46} When the nanopipette is cooled down before the pulling process of the second step, the glass capillary breaks during the second step, and a thicker glass nanopipette is fabricated (Figure 1d).

To miniaturize the nanopipette, fabrication guidelines are important. The first step of the borosilicate capillary fabrication process is used to adjust the ID/OD ratio of the glass capillary, which is related to the aperture size of the nanopipette. The

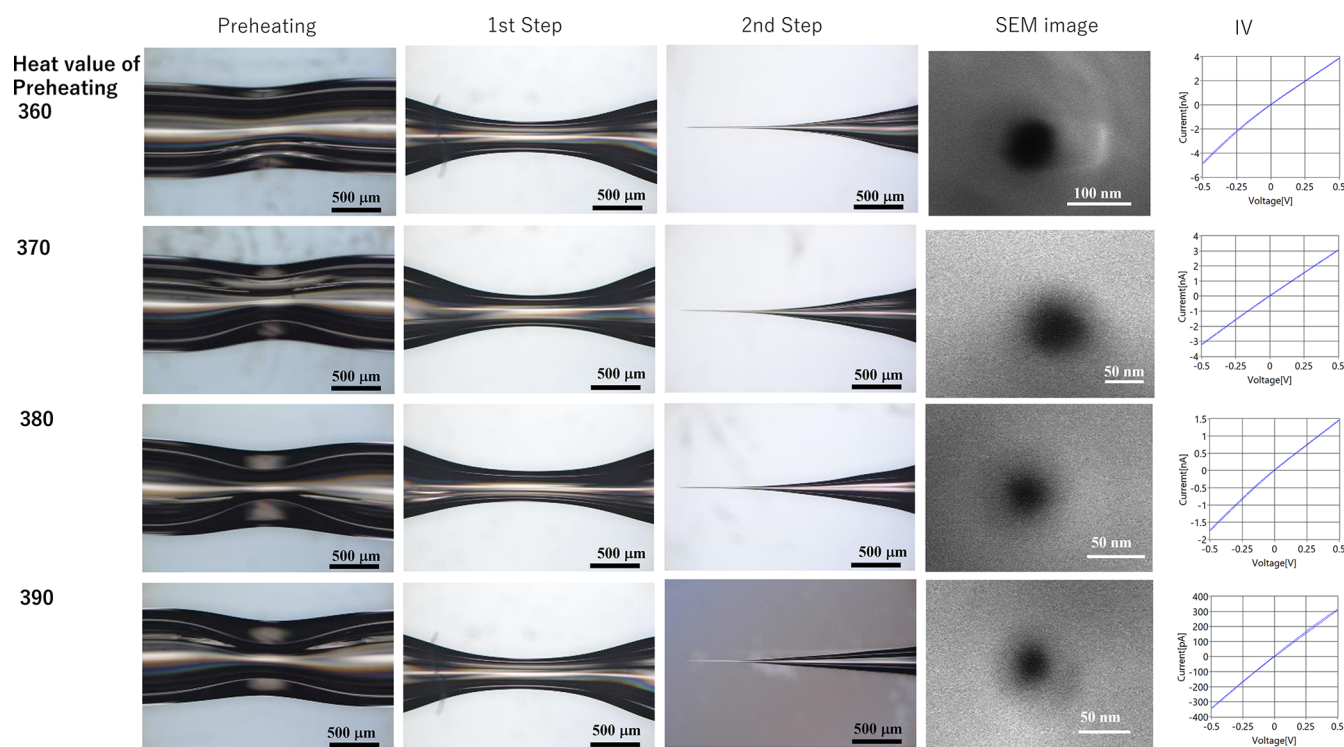


Figure 2. Controlling the ratio of the glass inner/outer thickness. Optical microscopy images, SEM images, and IV characteristics. IV characterization was performed in PBS (–) solution.

second step adjusts the sharpness of the glass. Although the parameters of the first step influence the size and reproducibility of the fabrication of nanopipettes, a comprehensive optimization of the fabrication parameters has not been reported yet. In addition, since commercially available glass capillaries do not come in a variety of ID/OD ratio, the control over the ID/OD ratio would be important to fabricate nanopipettes with the desired geometry.

To overcome this problem, we have established a method to adjust the ID/OD ratio of the glass in advance for fabricating sub-15 nm borosilicate nanopipettes with high reproducibility (Figure 1e). The ID/OD ratio was adjusted by heating the glass capillary for 5.0 s without stretching the capillary by keeping the pulley bars at a fixed position using a stopper in a P-2000 puller. We tested several heat values of the glass thinning step to optimize the inner/outer ratio. Figure 2 shows the optical microscopy images of the glass capillary after heating. The ID/OD ratio changed depending on the heat values. Then, we pulled the ID/OD-controlled borosilicate capillaries using a second step as described above. Figure 2 shows the optical microscopy (Nikon ECLIPSE LV100) and field emission SEM (Hitachi SU5000) images and the IV characteristics of the tip of the fabricated borosilicate glass nanopipettes. From the optical microscopy and SEM images, the differences in terms of the shape and length of the shunt and aperture radii can be observed. The pulling process of borosilicate capillaries preheated setting the heat parameter to 360, 370, 380, and 390 resulted in the fabrication of nanopipettes, showing a radius equal to 38, 29, 15, and 12 nm and resistances of 117, 155, 314, and 1527 M Ω , respectively. The fabrication reproducibility was characterized by IV curves (Figure S2). The relationship of the preheating value and the fabricated nanopipette radius is shown in Figure S3. The preheat values higher than 390 resulted in the melting

of the filament within the glass capillary, generating nanopipettes that were hard to fill with the electrolyte solution used for imaging.

In addition, the glass thickness at the tip is also an important factor for live cell nanoscale imaging without artifacts. In the case of patch clamp measurement, the PDMS coating at the top of the pipette has been used to increase the side glass wall resistance and reduce the capacitance at the tip of the pipette to enhance the signal-to-noise ratio.²⁸ Local heating of the tip of the nanopipette using SEM was also performed to shrink the glass wall to fabricate a small-aperture nanopipette.^{24,47} The pipette shape-dependent spatial resolution has been evaluated both theoretically and experimentally.^{7,48,49} A thick glass nanopipette has a disadvantage for SICM topography imaging because the outer glass wall of the tip of the nanopipette may deform the sample even when the ion current signal decrease does not reach the setpoint. Figure S1 shows the SICM images on the same region of the fixed HeLa cell using a thick [the nanopipette glass outer and inner radii ratio (RG) is more than 5.0] and thin glass (the RG is less than 2.0) nanopipette and typical thick and thin glass nanopipette SEM images. In the case of the thin glass nanopipette, the membrane ruffle can be clearly visualized, whereas in the case of thick glass, the topography of the ruffle was assessed to be concave with respect to the flat cell surface. This is because the deformed membrane ruffles are trapped between the nanopipette and the cell and prevented the tight packing between the nanopipette and the cell. In this case, the ion current did not change even if the nanopipette side wall contacts the cell surface. For this reason, SICM researchers are currently unable to visualize the cap formation process during clathrin-dependent endocytosis even if they could visualize the endocytic pit as a snapshot image. Therefore, a relatively thin glass nanopipette is preferred for SICM.

Time-Lapse Imaging of Endocytic Pit. To confirm the effectiveness of the fabricated nanopipettes for SICM topographic imaging, we imaged the same area of immobilized HeLa cells with the fine nanopipettes fabricated using the newly established method and with conventional nanopipettes (Figure 3). The pipette resistances were 412 and 261 M Ω ,

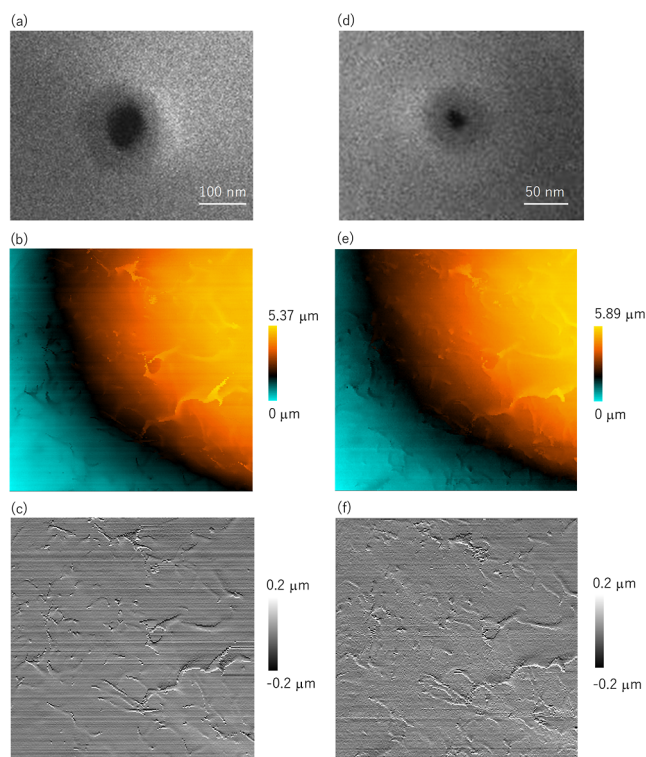


Figure 3. SICM topographic images of microvilli on a HeLa cell for evaluating the effect of nanopipette sizes. (a,d) SEM images of the tip of the nanopipette and (b,e) topographic images and (c,f) slope images of the conventional nanopipette and a miniaturized nanopipette, respectively. Scan sizes: $10 \times 10 \mu\text{m}^2$.

respectively. The slope images are also shown to facilitate the understanding of the small height change. The miniaturized nanopipette succeeded in capturing some small protrusion structures that could not be captured by a conventional pipette with an aperture diameter of 100 nm. Thus, the glass thickness obtained using the new nanopipette fabrication method does not introduce artifacts.

The nanopipette shape is also an important factor for a low-noise ion current measurement. The miniaturization of the nanopipette aperture is not so difficult and can be obtained by tuning the heat, velocity, pull, filament, and delay parameters of a P-2000 puller. However, the pipette resistance increases because of the long shunt length. Furthermore, the long shunt nanopipette causes the rectification effect, which interferes with the ion current measurement and decreases the steady-state ion current stability.^{44–46,50} This problem occurs when the glass is not sufficiently thinned during the first step of the elongation process. Since the thickness of the glass is excessively thick at the start time of the second step, the shunt of the nanopipette after being elongated in the second step becomes excessively long, resulting in a nanopipette showing a rectifying behavior. In this case, it can be resolved by increasing the velocity of the first step to make thinner glass capillaries at the first step. These results indicate that the shape

of the nanopipette is an important factor for steady ion current measurement.

Then, we observed the endocytic pit using a nanopipette with small aperture and thin glass walls obtained with the newly developed protocol. Figure 4a shows the results of the high-resolution imaging of fixed HeLa cells. The nanopipette resistance was 197 M Ω . In the hopping mode, the measurement of rough samples takes more time due to the longer vertical travel of the nanopipette, and it is more prone to artifacts due to the noise affecting the ion current. Therefore, the imaging region is generally limited to a very flat and small area on the cell surface, in most cases $7 \times 7 \mu\text{m}^2$, which enables the visualization of the endocytic pits. By using the nanopipette with a small aperture and thin glass walls, the endocytic pits and the microvilli on the cell surface were visualized simultaneously with a wide field of view of $20 \times 20 \mu\text{m}^2$, overcoming the limits imposed by the hopping mode. In addition, time-lapse imaging of the clathrin pit on live HeLa cells was also performed by using a borosilicate glass nanopipette (Figure 4b, supporting Movie S1). The nanopipette resistance was 286 M Ω . The imaging time was 36 s/frame. The cap formation to enclose the endocytosis cavity and the disappearance of the endocytic pit were visualized. This is the first time when a borosilicate glass nanopipette was used to visualize the cap formation during endocytosis.

Topographic Imaging of Released Small EVs. Confocal microscopy can be used to visualize the active releasing site of EVs, but it is difficult to identify and count individual EVs due to the diffraction limit. Electron microscopy allows the details of EVs to be seen. However, the fixation process required for electron microscopy can cause alterations in the EV shape. SICM can be used to visualize the topography of EVs in solution. In addition, SICM allows physiochemical information,⁵¹ such as charge, and sample surface stiffness⁵² to be obtained. The surface charge of individual EVs is also an important topic,⁵³ and differences in the expression state of negatively charged phosphatidylserine on the surface of EVs can be evaluated using SICM.

The nanopipette fabricated with the newly developed protocol is useful to visualize the nanoparticle's internalization and release. As a demonstration of the nanoparticle measurement, we imaged the small EVs and large EVs. The results are shown in Figure 5. The topographic images of the small EVs and large EVs can be captured clearly by SICM. These results suggest that SICM is effective to visualize the small EVs even in the case of highly convoluted surfaces. Then, we imaged the released EVs using SICM. Since EVs are released by exocytosis, which happens in less than a few tens of ms, it is difficult to capture the cell surface shape changes because of the temporal resolution of SICM imaging. Therefore, the released EVs were trapped on the Petri dish using the interaction of TIM4 and phosphatidylserine.⁵⁴ Confocal microscopy was used to confirm the trapped EVs on the Petri dish as a fluorescent signal of the Red Fluorochrome 635-anti CD63 antibodies. Figure 6 shows the confocal and SICM topographic images. The nanopipette resistance was 220 M Ω . From the confocal microscopy image, heterogeneous fluorescence signal distribution was observed around the cells on the Petri dish. Some regions showed high-density fluorescence signals, while others showed low-density fluorescence signals. Then, we imaged the regions showing a high-density fluorescent signal (Figure 6c) using SICM, and we compared it to the regions with a low-density fluorescence region (Figure

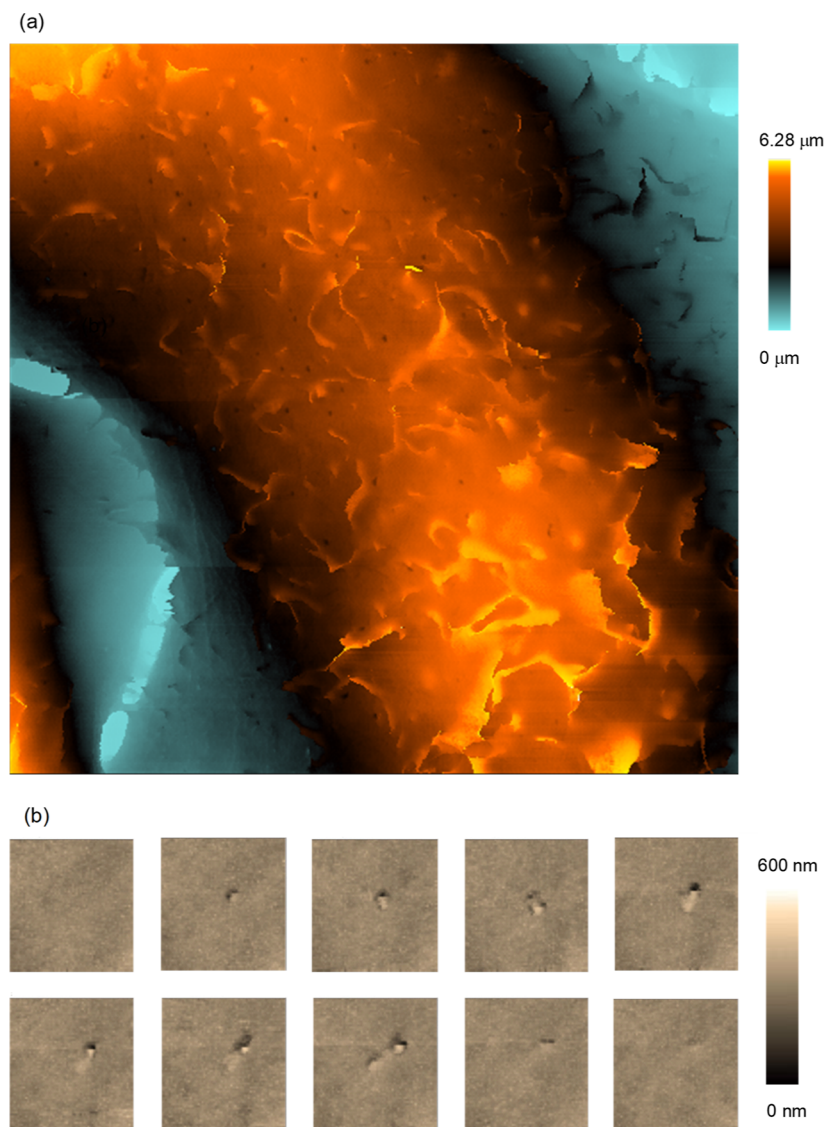


Figure 4. Topography images of the endocytic pit using SICM. (a) Fixed HeLa cell surface. (b) Live Cos7 cell time-lapse images. 36 s/frame. Scan sizes: (a) $20 \times 20 \mu\text{m}^2$ and (b) $2.5 \times 2.5 \mu\text{m}^2$. Pixel numbers: (a) 512×512 and (b) 64×64 .

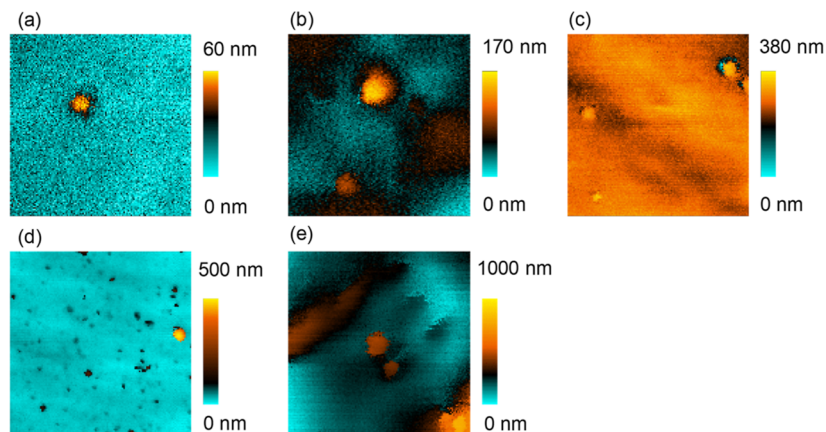


Figure 5. SICM topography images of small EVs on (a) dish, (b) fixed cell, (c) and live cell and large EVs on (d) dish and (e) fixed cell. Scan sizes: (a,b) $1 \times 1 \mu\text{m}^2$, (c) $2 \times 2 \mu\text{m}^2$, (d) $5 \times 5 \mu\text{m}^2$, and (e) $1.5 \times 1.5 \mu\text{m}^2$.

6d). In the high-fluorescence area, many trapped EVs could be visualized. The diameter of EVs was 189 nm from the SICM cross-section (Figure 6f). In the low-fluorescence area, almost

no EV was observed by SICM. These heterogeneity results suggest that the hot spot of the EV release was localized on the cell. Our newly developed protocol enables the measurement

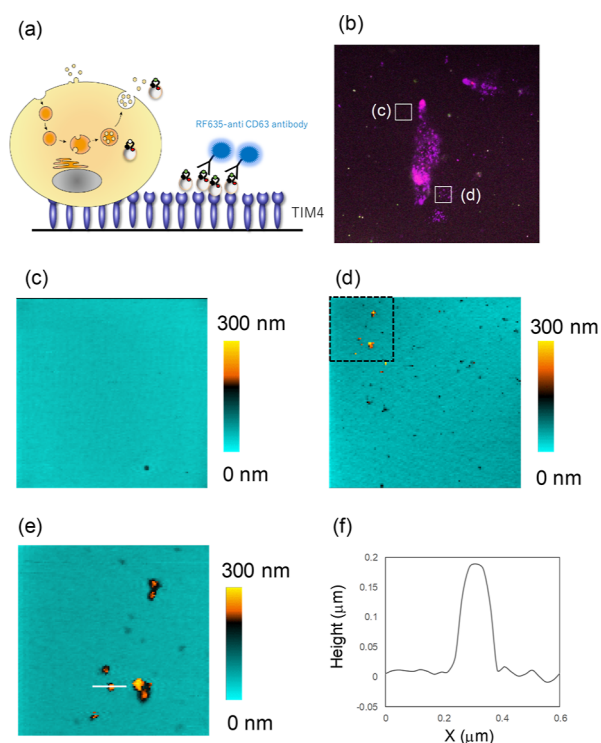


Figure 6. Released EV imaging by SICM: (a) schematic illustration of the fluorescent imaging of the released EVs. The fluorescent labeled EVs were trapped by TIM4. (b) Confocal microscopy image and SICM topography images of (c) no fluorescent signal region and (d) fluorescent signal region. (e) High magnification image of (d). Scan sizes: (c,d) $10 \times 9.8 \mu\text{m}^2$ and (e) $3.0 \times 3.0 \mu\text{m}^2$. (f) Cross-section on the white line of the topographic image of (e).

of biological entities with size below the diffraction limit of optical microscopy using a borosilicate nanopipette.

CONCLUSIONS

A simple method has been established for the highly reproducible production of small aperture and thin glass nanopipettes by controlling the glass ID/OD ratio by preheating the glass capillary. This method allows the ID/OD ratio of the glass to be freely adjusted, making it possible to create nanopipettes of various sizes. The control of the inner/outer thickness ratio of glass capillaries is also an important factor for fabricating sub-20 nm radius nanopipettes for high-resolution SICM imaging. We established the guidelines to control the glass thickness of borosilicate capillaries to fabricate nanopipettes with small apertures and short shunts. We used this technique to fabricate nanopipettes suitable for visualizing the nanoscale cell surface morphology changes and single small EVs during endocytosis/exocytosis. In addition, we combined SICM and confocal microscopy to visualize the hot spot of the EV release. We envision that this protocol will help to reproducibly fabricate borosilicate nanopipettes for high-resolution topographical mapping using SICM.

ASSOCIATED CONTENT

Supporting Information

The Supporting Information is available free of charge at <https://pubs.acs.org/doi/10.1021/acs.analchem.3c01010>.

Characterization of the relationship between nanopipette glass thickness and topographic image quality (PDF)

SICM time-lapse topographic imaging of the endocytosis process (MP4)

AUTHOR INFORMATION

Corresponding Author

Yasufumi Takahashi – Department of Electronics, Graduate School of Engineering, Nagoya University, Nagoya 464-8603, Japan; Nano Life Science Institute (WPI-NanoLSI), Kanazawa University, Kanazawa 920-1192, Japan; orcid.org/0000-0003-2834-8300; Email: takahashi.yasufumi.v5@f.mail.nagoya-u.ac.jp

Authors

Yuya Sasaki – Division of Electrical Engineering and Computer Science, Kanazawa University, Kanazawa 920-1192, Japan

Takeshi Yoshida – Nano Life Science Institute (WPI-NanoLSI), Kanazawa University, Kanazawa 920-1192, Japan

Kota Honda – Department of Electronics, Graduate School of Engineering, Nagoya University, Nagoya 464-8603, Japan

Yuanshu Zhou – Nano Life Science Institute (WPI-NanoLSI), Kanazawa University, Kanazawa 920-1192, Japan

Takafumi Miyamoto – Division of Electrical Engineering and Computer Science, Kanazawa University, Kanazawa 920-1192, Japan

Tomoko Motoo – Nano Life Science Institute (WPI-NanoLSI), Kanazawa University, Kanazawa 920-1192, Japan

Hiroki Higashi – Division of Electrical Engineering and Computer Science, Kanazawa University, Kanazawa 920-1192, Japan

Andrew Shevchuk – Department of Medicine, Imperial College London, London W12 0NN, U.K.

Yuri Korchev – Nano Life Science Institute (WPI-NanoLSI), Kanazawa University, Kanazawa 920-1192, Japan; Department of Medicine, Imperial College London, London W12 0NN, U.K.

Hiroki Ida – Department of Electronics, Graduate School of Engineering, Nagoya University, Nagoya 464-8603, Japan; orcid.org/0000-0002-1033-0033

Rikinari Hanayama – Nano Life Science Institute (WPI-NanoLSI), Kanazawa University, Kanazawa 920-1192, Japan

Takeshi Fukuma – Nano Life Science Institute (WPI-NanoLSI) and Division of Electrical Engineering and Computer Science, Kanazawa University, Kanazawa 920-1192, Japan; orcid.org/0000-0001-8971-6002

Complete contact information is available at: <https://pubs.acs.org/doi/10.1021/acs.analchem.3c01010>

Notes

The authors declare no competing financial interest.

ACKNOWLEDGMENTS

This work was supported by the World Premier International Research Center Initiative (WPI) from MEXT, Japan; the JST FOREST Program, grant nos. JPMJFR203K and JPMJFR214J; AMED under grant nos. JP21km0908001 and JP22gm1410012; JST Core Research for Evolutional Science

and Technology (CREST), grant no. JPMJCR18H4; a grant-in-aid for Scientific Research (A) (19H00993); a grant-in-aid for Scientific Research (B) (20H02582); and a grant-in-aid for Exploratory Research (22K18939) from the Japan Society for the Promotion of Science (JSPS). Y.T. was supported by the Takahashi Industrial and Economic Research Foundation; the Kurita Water and Environment Foundation; the Mitani Foundation for Research and Development; the Foundation for the Promotion of Ion Engineering; the Nakatani Foundation; the Novartis Research Foundation; and the CASIO Science Promotion Foundation. A.S. was supported by EPSRC UK (grants EP/W012219/1 and EP/R035571/1).

REFERENCES

- (1) Quinn, S. E.; Huang, L.; Kerkvliet, J. G.; Swanson, J. A.; Smith, S.; Hoppe, A. D.; Anderson, R. B.; Thies, N. W.; Scott, B. L. *Nat. Commun.* **2021**, *12*, 4838.
- (2) Chen, B. C.; et al. *Science* **2014**, *346*, 1257998.
- (3) Korchev, Y. E.; Bashford, C. L.; Milovanovic, M.; Vodyanoy, I.; Lab, M. J. *Biophys. J.* **1997**, *73*, 653–658.
- (4) Rheinlaender, J.; Geisse, N. A.; Proksch, R.; Schaffer, T. E. *Langmuir* **2011**, *27*, 697–704.
- (5) Ushiki, T.; Nakajima, M.; Choi, M.; Cho, S. J.; Iwata, F. *Micron* **2012**, *43*, 1390–1398.
- (6) Zhu, C.; Huang, K. X.; Siepser, N. P.; Baker, L. A. *Chem. Rev.* **2021**, *121*, 11726–11768.
- (7) Edwards, M. A.; Williams, C. G.; Whitworth, A. L.; Unwin, P. R. *Anal. Chem.* **2009**, *81*, 4482–4492.
- (8) Nikolaev, V. O.; Moshkov, A.; Lyon, A. R.; Miragoli, M.; Novak, P.; Paur, H.; Lohse, M. J.; Korchev, Y. E.; Harding, S. E.; Gorelik, J. *Science* **2010**, *327*, 1653–1657.
- (9) Novak, P.; Gorelik, J.; Vivekananda, U.; Shevchuk, A. I.; Ermolyuk, Y. S.; Bailey, R. J.; Bushby, A. J.; Moss, G. W. J.; Rusakov, D. A.; Klenerman, D.; Kullmann, D. M.; Volynski, K. E.; Korchev, Y. E. *Neuron* **2013**, *79*, 1067–1077.
- (10) Takahashi, Y.; Zhou, Y.; Miyamoto, T.; Higashi, H.; Nakamichi, N.; Takeda, Y.; Kato, Y.; Korchev, Y.; Fukuma, T. *Anal. Chem.* **2020**, *92*, 2159–2167.
- (11) Mann, S. A.; Hoffmann, G.; Hengstenberg, A.; Schuhmann, W.; Dietzel, I. D. *J. Neurosci. Methods* **2002**, *116*, 113–117.
- (12) Takahashi, Y.; Shevchuk, A. I.; Novak, P.; Zhang, Y. J.; Ebejer, N.; Macpherson, J. V.; Unwin, P. R.; Pollard, A. J.; Roy, D.; Clifford, C. A.; Shiku, H.; Matsue, T.; Klenerman, D.; Korchev, Y. E. *Angew. Chem., Int. Ed.* **2011**, *50*, 9638–9642.
- (13) Gorelik, J.; Zhang, Y. J.; Sanchez, D.; Shevchuk, A.; Frolenkov, G.; Lab, M.; Klenerman, D.; Edwards, C.; Korchev, Y. *Proc. Natl. Acad. Sci. U.S.A.* **2005**, *102*, 15000–15005.
- (14) Zhang, Y.; et al. *Nat. Commun.* **2019**, *10*, 5610.
- (15) Ida, H.; Takahashi, Y.; Kumatani, A.; Shiku, H.; Matsue, T. *Anal. Chem.* **2017**, *89*, 6016–6021.
- (16) Novak, P.; Li, C.; Shevchuk, A. I.; Stepanyan, R.; Caldwell, M.; Hughes, S.; Smart, T. G.; Gorelik, J.; Ostanin, V. P.; Lab, M. J.; Moss, G. W. J.; Frolenkov, G. I.; Klenerman, D.; Korchev, Y. E. *Nat. Methods* **2009**, *6*, 935.
- (17) Novak, P.; Shevchuk, A.; Ruenaroengsak, P.; Miragoli, M.; Thorley, A. J.; Klenerman, D.; Lab, M. J.; Tetley, T. D.; Gorelik, J.; Korchev, Y. E. *Nano Lett.* **2014**, *14*, 1202–1207.
- (18) Ida, H.; Takahashi, Y.; Kumatani, A.; Shiku, H.; Murayama, T.; Hirose, H.; Futaki, S.; Matsue, T. *Anal. Chem.* **2021**, *93*, 5383–5393.
- (19) Shevchuk, A. I.; Hobson, P.; Lab, M. J.; Klenerman, D.; Krauzewicz, N.; Korchev, Y. E. *Pflugers Arch.* **2008**, *456*, 227–235.
- (20) Hagemann, P.; Gesper, A.; Happel, P. *ACS Nano* **2018**, *12*, 5807–5815.
- (21) Boschini, F.; Leitao, S. M.; Grussmayer, K. S.; Descloux, A.; Drake, B.; Yserentant, K.; Werther, P.; Herten, D. P.; Wombacher, R.; Radenovic, A.; Fantner, G. E. *Nat. Commun.* **2021**, *12*, 597.
- (22) Prestopino, G.; Watanabe, S.; Ando, T. *Appl. Phys. Lett.* **2017**, *111*, 111105.
- (23) Simeonov, S.; Schäffer, T. E. *Nanoscale* **2019**, *11*, 8579–8587.
- (24) Leitao, S. M.; Drake, B.; Pinjusic, K.; Pierrat, X.; Navikas, V.; Nievergelt, A. P.; Brillard, C.; Djekic, D.; Radenovic, A.; Persat, A.; Constam, D. B.; Anders, J.; Fantner, G. E. *ACS Nano* **2021**, *15*, 17613–17622.
- (25) Shevchuk, A. I.; Novak, P.; Taylor, M.; Diakonov, I. A.; Ziyadeh-Isleem, A.; Bitoun, M.; Guicheney, P.; Lab, M. J.; Gorelik, J.; Merrifield, C. J.; Klenerman, D.; Korchev, Y. E. *J. Cell Biol.* **2012**, *197*, 499–508.
- (26) Bednarska, J.; Pelchen-Matthews, A.; Novak, P.; Burden, J. J.; Summers, P. A.; Kuimova, M. K.; Korchev, Y.; Marsh, M.; Shevchuk, A. *Proc. Natl. Acad. Sci. U.S.A.* **2020**, *117*, 21637–21646.
- (27) Shevchuk, A. I.; Frolenkov, G. I.; Sanchez, D.; James, P. S.; Freedman, N.; Lab, M. J.; Jones, R.; Klenerman, D.; Korchev, Y. E. *Angew. Chem., Int. Ed.* **2006**, *45*, 2212–2216.
- (28) Levis, R. A.; Rae, J. L. *Biophys. J.* **1993**, *65*, 1666–1677.
- (29) Salançon, E.; Tinland, B. *Beilstein J. Nanotechnol.* **2018**, *9*, 2181–2187.
- (30) Sun, L.; Shigyou, K.; Ando, T.; Watanabe, S. *Anal. Chem.* **2019**, *91*, 14080–14084.
- (31) Navikas, V.; Leitão, S. M.; Marion, S.; Davis, S. J.; Drake, B.; Fantner, G. E.; Radenovic, A. *ACS Appl. Nano Mater.* **2020**, *3*, 7829–7834.
- (32) Raposo, G.; Stoorvogel, W. *J. Cell Biol.* **2013**, *200*, 373–383.
- (33) Thery, C.; Ostrowski, M.; Segura, E. *Nat. Rev. Immunol.* **2009**, *9*, 581–593.
- (34) Thery, C.; et al. *J. Extracell. Vesicles* **2018**, *7*, 1535750.
- (35) Chen, C.; Zong, S.; Wang, Z.; Lu, J.; Zhu, D.; Zhang, Y.; Cui, Y. *ACS Appl. Mater. Interfaces* **2016**, *8*, 25825–25833.
- (36) Koliha, N.; Wiencek, Y.; Heider, U.; Jüngst, C.; Kladt, N.; Krauthäuser, S.; Johnston, I. C. D.; Bosio, A.; Schauss, A.; Wild, S. *J. Extracell. Vesicles* **2016**, *5*, 29975.
- (37) Hardij, J.; Cecchet, F.; Berquand, A.; Gheldof, D.; Chatelain, C.; Mullier, F.; Chatelain, B.; Dogné, J.-M. *J. Extracell. Vesicles* **2013**, *2*, 21045.
- (38) Palanisamy, V.; Sharma, S.; Deshpande, A.; Zhou, H.; Gimzewski, J.; Wong, D. T. *PLoS One* **2010**, *5*, No. e8577.
- (39) Yurtsever, A.; Yoshida, T.; Badami Behjat, A.; Araki, Y.; Hanayama, R.; Fukuma, T. *Nanoscale* **2021**, *13*, 6661–6677.
- (40) Shirasaki, Y.; Yamagishi, M.; Suzuki, N.; Izawa, K.; Nakahara, A.; Mizuno, J.; Shoji, S.; Heike, T.; Harada, Y.; Nishikomori, R.; Ohara, O. *Sci. Rep.* **2014**, *4*, 4736.
- (41) Zhou, Y. S.; Saito, M.; Miyamoto, T.; Novak, P.; Shevchuk, A. I.; Korchev, Y. E.; Fukuma, T.; Takahashi, Y. *Anal. Chem.* **2018**, *90*, 2891–2895.
- (42) Takahashi, Y.; Murakami, Y.; Nagamine, K.; Shiku, H.; Aoyagi, S.; Yasukawa, T.; Kanzaki, M.; Matsue, T. *Phys. Chem. Chem. Phys.* **2010**, *12*, 10012–10017.
- (43) Yoshida, T.; Ishidome, T.; Hanayama, R. *Curr. Protoc. Cell Biol.* **2017**, *77*, 3.45.1–3.45.18.
- (44) Powell, M.; Healy, K.; Davenport, M.; Niya, S.; Baker, L.; Letant, S.; Siwy, Z. *Biophys. J.* **2011**, *100*, 609.
- (45) Powell, M. R.; Vlassiouk, I.; Martens, C.; Siwy, Z. S. *Phys. Rev. Lett.* **2009**, *103*, 248104.
- (46) Hoogerheide, D. P.; Garaj, S.; Golovchenko, J. A. *Phys. Rev. Lett.* **2009**, *102*, 256804.
- (47) Steinbock, L. J.; Steinbock, J. F.; Radenovic, A. *Nano Lett.* **2013**, *13*, 1717–1723.
- (48) Rheinlaender, J.; Schaffer, T. E. *J. Appl. Phys.* **2009**, *105*, 094905 DOI: 10.1063/1.3122007.
- (49) Weber, A. E.; Baker, L. A. *J. Electrochem. Soc.* **2014**, *161*, H924–H929.
- (50) Umehara, S.; Pourmand, N.; Webb, C. D.; Davis, R. W.; Yasuda, K.; Karhanek, M. *Nano Lett.* **2006**, *6*, 2486–2492.
- (51) Klausen, L. H.; Fuhs, T.; Dong, M. D. *Nat. Commun.* **2016**, *7*, 12447.
- (52) Kolmogorov, V. S.; Erofeev, A. S.; Woodcock, E.; Efremov, Y. M.; Iakovlev, A. P.; Savin, N. A.; Alova, A. V.; Lavrushkina, S. V.; Kireev, I. I.; Prelovskaya, A. O.; et al. *Nanoscale* **2021**, *13*, 6558–6568.

(53) Deregibus, M. C.; Figliolini, F.; D'antico, S.; Manzini, P. M.; Pasquino, C.; De Lena, M.; Tetta, C.; Brizzi, M. F.; Camussi, G. *Int. J. Mol. Med.* **2016**, 38, 1359–1366.

(54) Nakai, W.; Yoshida, T.; Diez, D.; Miyatake, Y.; Nishibu, T.; Imawaka, N.; Naruse, K.; Sadamura, Y.; Hanayama, R. *Sci. Rep.* **2016**, 6, 33935.

■ NOTE ADDED AFTER ISSUE PUBLICATION

This paper was originally published ASAP on August 21, 2023. Due to a production error, the y-axis labels in the graphs of Figure 2 contained a typo. The corrected version was reposted on September 1, 2023.